# Air plasma sprayed Cu–Co–GDC anode coatings with various Co loadings

Nir Light [a], Olivera Kesler [b,*]

[a] Department of Mechanical Engineering, The University of British Columbia, 2054-6250 Applied Sciences Lane, Vancouver, British Columbia, Canada V6T 1Z4
[b] Department of Mechanical and Industrial Engineering, University of Toronto, 5 King's College Road, Toronto, Ontario, Canada M5S 3G8

## HIGHLIGHTS

► Plasma spraying was used to manufacture Cu–Co–GDC coatings for use in SOFC anodes.
► Coating composition was set using the absolute deposition efficiencies.
► Co does not seem to have a role in increasing coating porosity.
► XRD patterns indicated possible interdiffusion of Co and Cu.
► The coatings demonstrated stability against carbon formation comparable to that in literature.

## ARTICLE INFO

## ABSTRACT

In this work, Cu–Co–gadolinia doped ceria (GDC) anode coatings were fabricated by atmospheric plasma spraying (APS) of agglomerated CuO, $Co_3O_4$, and GDC feedstock powders. Screening tests were conducted to identify the effect of plasma gas composition on the coating phases, microstructure, and absolute deposition efficiency of each material. Based on screening tests, optimized plasma energy conditions were identified. Using the absolute deposition efficiency, feedstock powder mixing ratios were determined to produce anode coatings with Cu–Co weight ratios of Cu(100)–Co(0), Cu(90)–Co(10), Cu(70)–Co(30), and Cu(50)–Co(50), with 40 vol% of metal phases in the coating and 60 vol% of GDC. After reduction of the coatings, porosity and gas permeability were determined. Finally, carbon deposition behavior was examined by measuring the weight gain of the coatings after exposure to $CH_4$ at 700 °C for 3 h. The coatings demonstrated good resistance to carbon deposition.

© 2013 Elsevier B.V. All rights reserved.

## 1. Introduction

Solid oxide fuel cells (SOFCs) are electrochemical energy conversion devices that have drawn attention due to their low pollution, high energy efficiency, and their ability to utilize hydrocarbon (HC) fuels. Operation on hydrocarbon fuels such as methane rather than pure hydrogen may accelerate the commercialization of SOFC systems due to the readily available infrastructure for such fuels.

Commonly, HC fuels are utilized internally in SOFCs with typical Ni-YSZ (yttria stabilized zirconia) anodes by steam reforming and water gas-shift, or an external reformer is used to process the fuel. However, these methods have technological issues [1] that limit their use, which drives current attempts to utilize HC with a direct oxidation mechanism using coking-resistant Cu-based anodes [1–4]. In

these anodes, Cu does not appear to have any catalytic function, and the oxidation reaction at the triple phase boundaries relies on the addition of other components, such as ceria [5,6] or Co [7–10].

Co–Cu bimetallic anodes processed by impregnation of aqueous metal salts into pre-sintered porous YSZ structures have demonstrated increased performance and better thermal stability in comparison to Cu-based anodes, without severe carbon deposition [7]. In these anodes, the Cu and Co do not form a bulk solid solution, but rather exist in the form of two separate phases. It has been suggested that the resistance toward carbon deposition is achieved by surface alloying of Cu and Co coupled with segregation of Cu at the Cu–Co surface, resulting in suppressed carbon formation even with Cu–Co compositions containing small amounts of Cu. Cells produced with a 50–50 Cu–Co ratio (by weight) in the metallic phases demonstrated no degradation in performance after a 500 h test with $CH_4$ [7].

Until recently, Cu based anodes have been processed by multistep wet ceramic processes such as impregnation of aqueous

metal salts into pre-sintered porous YSZ structures. However, the multiple infiltration and firing steps required to achieve adequate loading of the metal phase(s) make wet ceramic processes non-ideal for mass production. This and other problems with wet ceramic processing have driven recent attempts to utilize plasma spraying to produce SOFCs [14]. Plasma spraying has several advantages, such as high production rates, reduced costs for low-volume and high-volume production, ease of automation, elimination of high-temperature sintering steps, which creates a greater choice of cell fabrication materials, facilitation of the use of metallic supports, and the manufacturing of cell layers in one integrated process [14]. Cu–SDC anodes [1] and Cu–Co–YSZ layers [11,12] have been produced recently by atmospheric plasma spraying.

Recently, we demonstrated the application of atmospheric plasma spraying to produce Cu–samaria doped ceria (SDC) anode layers manufactured from micron-sized CuO and SDC agglomerated feedstocks. The SDC in these anodes enhances catalytic activity and increases performance, as demonstrated by other studies [4], as well as suppressing the sintering of the Cu. CuO was utilized as a feedstock due to the porosity gain when the CuO is reduced to Cu. In addition, CuO has a higher melting temperature than Cu, and therefore, it may be easier to co-deposit with a higher melting temperature material such as SDC. Finally, micron-sized agglomerated powder was utilized to increase anode surface area, as in other studies [13].

In this work, we present the use of APS processing for the manufacturing of Cu–Co–GDC (gadolinia doped ceria, $Ce_{0.8}Gd_{0.2}O_{1.9}$) SOFC anode layers utilizing micron-sized agglomerated CuO, CoO, and GDC feedstock powders. We present the spraying and feedstock parameters developed and used to deposit CoO–CuO–GDC SOFC anode layers with different Co loadings and the resulting deposition efficiencies, elemental compositions, crystal structures, microstructures, and tolerance toward carbon deposition.

## 2. Experimental procedure

### 2.1. Material preparation

In this work, commercially available feedstock powders of CuO, $Co_3O_4$, and GDC (Inframat Advanced Materials, Farmington, CT, USA) were used to produce the coatings. These powders were spherical spray dried agglomerates of sub-micron powder.

In order to prevent the breakup of the spray dried agglomerates during feeding, the CuO and GDC as-received powders were calcined at various temperatures to enhance cohesion. Table 1 shows the particle size distribution and calcining time and temperature of the calcined powders. The calcined powders were then sieved into narrower size fractions, with the sieved powder in the sieve fraction size range of 32–45 μm being used for the plasma spraying experiments.

### 2.2. Plasma spray processing

Atmospheric plasma spraying of CuO–CoO–GDC coatings was implemented with an Axial III plasma torch (Northwest Mettech Corp., North Vancouver, BC, Canada) and a $N_2$–Ar plasma using a rotating drum sample holder and vertically rastering torch robot (additional details in [1]). Ar was used as the carrier gas. In order to allow good adhesion of the plasma sprayed coatings, substrates were pre-heated to 300 °C by the torch prior to deposition. Substrate temperature was monitored during the spraying process to ensure that it did not exceed 500 °C.

Preliminary screening tests were carried out with CuO, CoO, and GDC powders. The plasma gas composition was varied in the production of each of the coatings. Deposition was carried out onto

**Table 1**
Particle size distribution and calcining temperature and time of calcined powders.

| Powder | Particle size [μm] | | | Calcining temperature [°C] | Calcining time [h] |
|---|---|---|---|---|---|
| | $D_{0.1}$ | $D_{0.5}$ | $D_{0.9}$ | | |
| CuO | 14.5 | 34.5 | 61.6 | 850 | 5 |
| $Co_3O_4$[a] | 17.1 | 38.4 | 70.2 | 1100 | 5 |
| GDC | 23.3 | 36.7 | 58.0 | 1350 | 5 |

[a] $Co_3O_4$ decomposes to CoO when heated above 950 °C.

commercially available 2.54 cm diameter porous SS430 disk substrates (media grade 2, Mott Corporation, Farmington, CT, USA) with a thickness of approximately 1 mm. Table 2 shows experimental APS process parameters used for all coatings. Table 3 shows experimental APS process parameters varied for each different coating.

Following the identification of the range of suitable plasma and feedstock parameters, CuO–CoO–GDC coatings were deposited onto commercially available 2.54 cm diameter, 1.6 mm thick Cu disk substrates for carbon deposition tests, and on the SS430 porous substrates for gas permeability and porosity characterization. Initial powder weight ratios were determined for each of the coatings to obtain a Co weight fraction in the Cu–-Co phases of 0, 0.1, 0.3, and 0.5, and a volume fraction of approximately 40% of the metallic phases in the coating. After deposition, the coatings were reduced in a $N_2$–$H_2$ mixture (50% $H_2$) at 700 °C for 6 h.

### 2.3. Coating characterization

X-ray diffraction (XRD) analysis of the coatings was performed both before and after reduction to determine the phase structure dependence on spraying and feedstock parameters. When the extent of peak shift had to be identified with high accuracy to avoid errors resulting from tilting or misalignment of the sample, $Al_2O_3$ powder was put on the coatings and used for calibration of the x-ray detector position.

Energy dispersive x-ray spectroscopy (EDX) was performed to determine the composition of the coatings.

The porosity of the coatings was characterized by image analysis. Coatings were mounted in epoxy resin, sectioned, and polished. To minimize pull-out, which introduces errors in the calculated porosity, coatings were examined by optical microscopy between each polishing step. Polished cross-section images of each coating were taken with a scanning electron microscope (SEM, S3500N, Hitachi High Technologies America, Pleasanton, CA). Ten images were taken for each coating, at 0.50 mm intervals along the length of the coating. The images were taken at 3000× magnification, with corresponding analysis areas of 42.7 × 32.0 $\mu m^2$. To clearly distinguish between solid and pore when image analysis software is utilized, image brightness was reduced and contrast increased to create SEM images predominated by black and white, with minimal areas of grey. Image analysis was performed utilizing ImageJ software (National Institutes of Health, USA). An image

**Table 2**
Experimental APS process parameters used for all coatings.

| Parameter | Value |
|---|---|
| Carrier gas flow rate (slpm) | 15 |
| Spraying distance (mm) | 100 |
| Vertical traverse speed (ms$^{-1}$) | 4.25 |
| Torch current (A) | 690 |
| Plasma gas flow rate (slpm) | 250 |
| Nozzle size (mm) | 12.7 |
| CuO, CoO, and GDC particle sieve fraction size (μm) | −45 μm + 32 μm |

**Table 3**
Experimental APS process parameters used for coating fabrication.

| Parameter | Value | | | | |
|---|---|---|---|---|---|
| | Screening tests | Cu–GDC | 10 wt% Co | 26 wt% Co | 50 wt% Co |
| Powder feed rate (g min$^{-1}$) | 31.5 | 36.1 | 24.1 | 20.9 | 25.5 |
| Powder feed time (sec) | 38.0 | 99.8 | 70.0 | 100 | 100 |
| Vol.% N$_2$ (balance Ar) | 20, 40, 60, 80 | 40 | 40 | 40 | 40 |
| Torch power (kW) | 49.9, 60.6, 74.3 and 99.2 | 60.6 | 60.6 | 60.6 | 60.6 |
| Powder composition (wt%) | 33.3 GDC 33.3 CuO 33.3 CoO | 45.2 GDC 54.8 CuO | 54.8 GDC 40.3 CuO 5.0 CoO | 55.2 GDC 28.5 CuO 16.3 CoO | 53.9 GDC 21.0 CuO 25.2 CoO |

analysis procedure was developed that included determination of the likely range of porosity values and optimized most likely porosity value. The minimum likely porosity value was determined by setting a grey scale threshold such that no solid phases that could be identified visually in the coating were included within the threshold. The maximum likely porosity value was determined by setting a grey scale threshold such that all pores that could be identified visually were included within the threshold for calculated porosity. The most likely porosity value was determined by setting the grey scale threshold such that it corresponds well with the extent of the pore phase that can be visually identified.

Helium permeation measurements were performed using an in-house designed jig in order to determine the gas permeability of the deposited layers. The supply of helium gas was regulated by a pressure controller (Alicat Scientific, model PCD-5PSIG-D, Tucson, AZ, USA). The flow through the sample was then measured at the outlet of the jig by a mass flow meter (Alicat Scientific, model MC-500SCCM-D/5M 5IN N$_2$, Tucson, AZ, USA). To determine the thickness required for the permeability coefficient calculations, fifteen SEM images were taken at equal intervals of 0.5 mm along the coating cross-section length. Fig. 1 schematically depicts the gas permeability measurement set-up.

### 2.4. Carbon deposition

Carbon deposition was analyzed by measuring the weight gain of CuO-GDC and CuO–CoO-GDC coatings plasma sprayed onto 2.54 mm diameter Cu disks and exposed to 100% CH$_4$ at 700 °C. First, the coatings were reduced and the reduced coating weight was measured. Then, the coatings were heated in an 80% N$_2$/20% H$_2$ mixture at a rate of 1 °C min$^{-1}$ to 700 °C and then exposed to dry 100% CH$_4$ for 3 h. The 3 h exposure time was chosen to allow comparison of the carbon deposition data in this study to other studies appearing in the literature utilizing wet-ceramic processed Cu–Co–ceria coatings [7]. After exposure to CH$_4$, the gas mixture

was changed to a reducing mixture of 99.5% N$_2$/0.5% H$_2$ and the coatings were cooled at a rate of 1 °C min$^{-1}$ to room temperature and weighed. SEM analysis of the coatings was performed to detect carbon residue.

## 3. Results and discussion

### 3.1. Powder morphology

To determine the effect of the calcining step on the agglomerated powder, the calcined powder was examined by SEM. Fig. 2 shows SEM micrographs of the spray dried powder agglomerates after the calcining step. The primary particles are coarser relative to as those in the as-received (non-calcined) agglomerates. The primary particle size increased from sub-micron to approximately 3 µm for CuO, 5–10 µm for CoO, and 1 µm for GDC.

### 3.2. Microstructural analysis

#### 3.2.1. Microstructural analysis of screening test coatings

Fig. 3 shows XRD patterns of coatings produced from CuO–CoO–GDC feedstock powders. The crystal structure of the GDC in the coatings was cubic fluorite over the entire range of spraying conditions. This result is similar to results obtained with SDC powder [1]. Partial reduction of CuO to Cu$_2$O cannot be detected in the pattern because the Cu$_2$O and CoO peaks overlap.

The main difficulty in co-depositing CuO, CoO, and GDC composite coatings by APS is achieving sufficient porosity. The large difference between the melting temperature of CuO and GDC (1227 °C for CuO and 2480 °C for ceria [15]) makes it difficult to co-deposit these materials with sufficient porosity for optimized anode performance. In our previous work [1], it was demonstrated that the CuO almost completely melts in-flight for a wide range of APS parameters tested, even with low energy plasmas. Therefore, the strategy applied here to obtain sufficiently porous coatings is to identify APS parameters that will lead to partial melting of the GDC. Partial melting of the agglomerated GDC particles allows increased porosity, and in addition, allows the GDC to keep its finely structured morphology to some extent, which increases the anode surface area and improves its performance. This is especially important due to the dual role of doped ceria in Cu-doped ceria anodes, in which the Cu only plays a role as an electronic conductor, while the doped ceria functions as the catalyst toward oxidation of H$_2$ and CH$_4$ as well as a mixed ionic-electronic conductor [16].

An additional challenge in co-depositing CuO–CoO–GDC coatings is achieving the desired relative solid volume of metallic phases of 40% in the coating to allow full percolation of the metallic phases and thus to obtain sufficient electronic conductivity of the anode. Finally, spraying parameters must allow the CuO and CoO to be sufficiently melted to allow fine-scale mixing and possible covering of the Co by Cu after the CuO and CoO have been reduced.
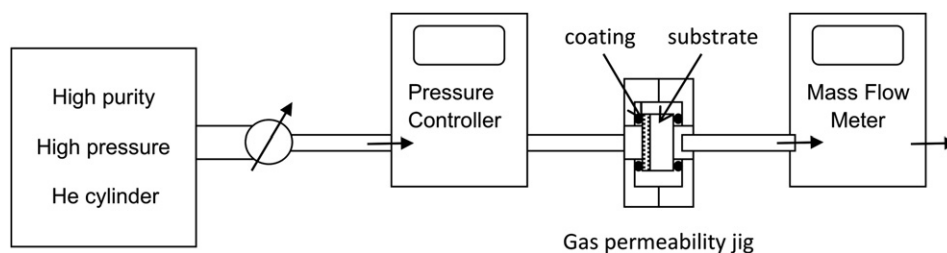


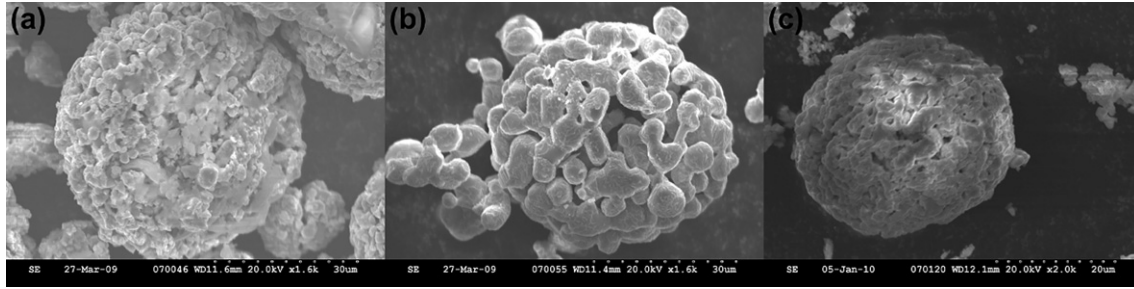**Fig. 1.** Gas permeability measurement set-up.

**Fig. 2.** SEM images of calcined (a) CuO, (b) CoO, and (c) GDC spray dried powders.

APS is a manufacturing process in which the feedstock powder is injected into the plasma jet, where powder particles absorb thermal and kinetic energy from the plasma jet and are then deposited onto a substrate in a fully or partially molten state to form a coating. Particle temperature and velocity in the plasma affect how well the powder is deposited. These conditions vary according to the physical properties of the plasma sprayed material, such as its melting temperature and heat capacity. Insufficiently melted plasma sprayed particles will bounce off the substrate upon impact, thus resulting in a lower absolute deposition efficiency. In the case of high energy plasmas, particles may evaporate or volatize, thus resulting in a lower deposition efficiency. Due to the differences between the melting temperatures, densities, and heat capacities of the CuO, CoO, and GDC materials, each of these materials will have a specific deposition efficiency for given set of spraying parameters, which is calculated for each material as the weight ratio between the powder deposited onto the substrate per unit area of the substrate times the area over which powder is delivered to the drum and the powder fed to the plasma torch, as seen in Eq (1).

$$\text{Absolute D.E} = \frac{\Delta W_{\text{substrate}} A_{\text{drum}}}{W_{\text{powder}} A_{\text{substrate}}} X_i \qquad (1)$$

where $\Delta W_{\text{substrate}}$ is the substrate weight gain, $W_{\text{powder}}$ is the weight of the fed powder, $A_{\text{drum}}$ is the total sprayed area, $A_{\text{substrate}}$ is the substrate area, and $X_i$ is the weight percent of material $i$ in the coating. $X_i$ is determined in this study by EDX analysis of the coating.

Using the deposition efficiencies of the materials, the initial powder ratios were adjusted to control the composition of the APS coatings and thus to obtain the desired metallic volume fraction of 40 vol% and also to obtain the desired weight ratios of the Cu and Co in the coatings.

Fig. 4 shows the plasma torch power versus the $N_2$ content in the plasma gas and the absolute deposition efficiencies of the GDC, CuO, and CoO as a function of the $N_2$ content in the plasma gas. It can be seen that the torch power increases with increasing $N_2$ content in the plasma gas. Previous studies showed that augmenting the $N_2$ content in the $N_2$–Ar plasma gas will increase the arc voltage and heat transfer ability of the plasma jet and consequently, the plasma power and particle temperature ([17]).

The absolute deposition efficiencies of the GDC, CuO, and CoO as a function of the $N_2$ content in the plasma gas are shown in Fig. 4. In plasma spray processing, lower deposition efficiencies can result from high vaporization rates of the deposited materials or from material rebound, which occurs when the particles have only
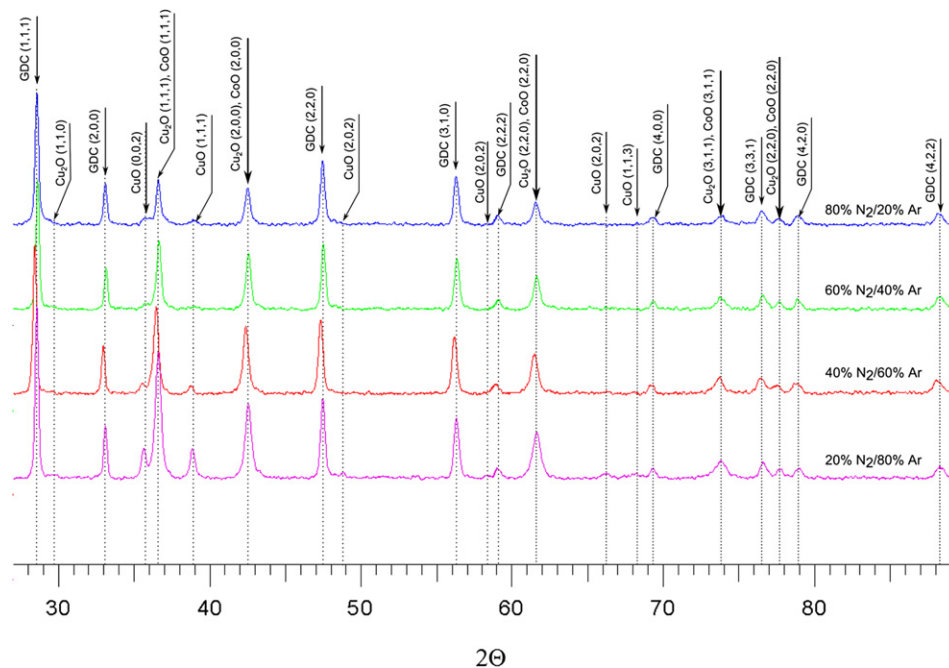


**Fig. 3.** XRD of CuO–CoO–GDC coatings produced with plasma gases having a $N_2$ content of (a) 20% (b) 40% (c) 60% and (d) 80% (balance Ar).
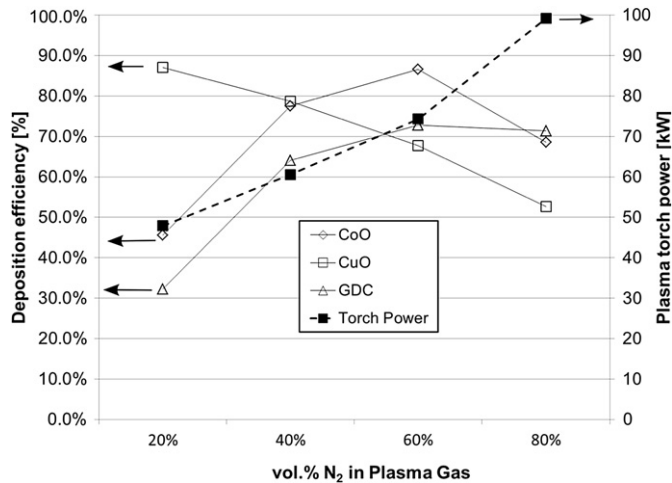
**Fig. 4.** Effect of the $N_2$ content in the plasma on the plasma torch power and absolute deposition efficiencies of CuO, CoO and GDC plasma sprayed with different plasma gas compositions.

**Table 4**
Relative volume of metallic phases in the coatings and relative weight of Co in the Cu–Co phases.

| Parameter | Cu–GDC | 10 wt% Co | 26 wt% Co | 50 wt% Co |
|---|---|---|---|---|
| Atomic fraction (obtained by EDX) (mol. %) | 74.5 Cu 24.1 Ce 5.50 Gd | 8.53 Co 64.5 Cu 21.7 Ce 5.80 Gd | 18.7 Co 48.9 Cu 26.3 Ce 6.00 Gd | 37.9 Co 35.5 Cu 21.2 Ce 5.30 Gd |
| Volume fraction of metallic phases in coating after reduction (vol. %) | 41.2 | 44.4 | 37.7 | 44.5 |
| Co content within metallic phases (wt. %) | N/A | 10.4 | 26.2 | 49.8 |

### 3.2.2. Microstructural analysis of Cu–Co–GDC coatings

Based on the absolute deposition efficiency of GDC and SEM of coatings obtained during the screening tests, a plasma gas composition of 40% $N_2$/60% Ar was used for subsequent coating deposition to allow sufficient melting of the CuO and CoO so that they can inter-diffuse to obtain resistance to carbon deposition, as suggested by wet-ceramic processed anode results reported elsewhere [7]. In addition, this plasma gas composition was chosen to allow deposition of partially-melted GDC particles with an absolute deposition efficiency of 64%. Due to the high cost of agglomerated GDC, it is desirable to utilize APS conditions that maximize the deposition efficiency of GDC subject to other constraints, such as the need to introduce adequate porosity. Moreover, the screening experiments demonstrated that a lower $N_2$ content in the plasma resulted in more homogenous coatings than the higher $N_2$ content. Using the absolute deposition efficiency, feedstock powder ratios were determined to produce CuO–CoO–GDC coatings with Co content of 0%, 10%, 30% and 50% by weight in the Cu–Co phases. The coatings were produced utilizing the spraying conditions shown in Tables 2 and 3. Energy dispersive X-ray spectroscopy (EDX) was performed on the coatings to determine the volume fraction of Cu and Co present in the coatings and the weight ratios of the Cu and Co; the results are shown in Table 4. Due to the presence of oxygen in all sprayed materials, EDX was performed to quantify atomically the Ce, Cu, and Co. Then, using the physical properties of the materials, the relative volumes and weights of Cu, Co, and GDC in the coatings were determined. The volume fractions and weight ratios were close to the targeted values.

Fig. 6 shows cross section SEM micrographs of coatings produced with (a) Cu–GDC, (b) 10 wt% Co, (c) 26 wt% Co, and (d) 50 wt % Co in the metallic phases. The non-conductive GDC appears lighter in SEM images, while the conductive Cu and Co appear darker. It can be seen that the anode materials are well mixed and that the GDC particles were partially melted in flight, thus
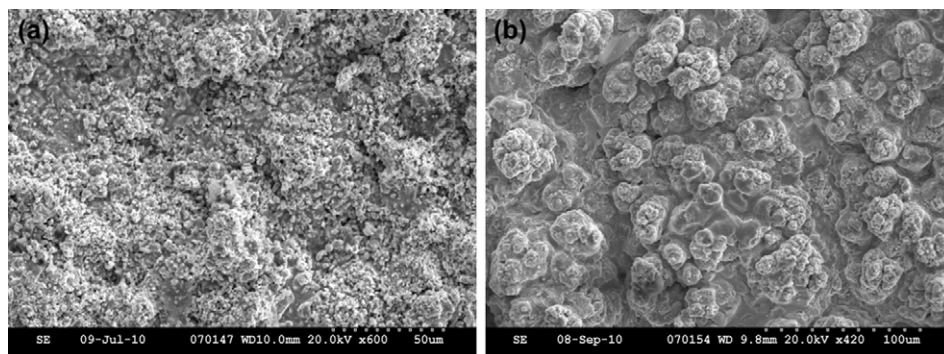
partially melted or have re-solidified prior to impact. It can be observed that the deposition efficiency of the CuO decreases with the increase of $N_2$ content in the plasma gas throughout the entire range of plasma gas composition examined. This decrease can be attributed to partial evaporation of the CuO during flight. The deposition efficiencies of the CoO and the GDC increase sharply when the $N_2$ content in the plasma is changed from 20% to 40%, and then more gradually when the $N_2$ content in the plasma is changed from 40% to 60%. This result can be attributed to a higher degree of melting of these materials with the increase of plasma energy. When the $N_2$ content is changed from 60% to 80%, a decrease of the deposition efficiencies of the CoO and the GDC is observed. This result may be attributable to increased plasma velocity, resulting in decreased residence time of the particles in the plasma, or to higher evaporation rates of these materials due to the higher plasma energy with 80% $N_2$.

Fig. 5 shows surface SEM micrographs of coatings produced with 40% $N_2$ and 80% $N_2$. The coating produced with 40% $N_2$ is homogenous and the fine structure of the GDC particles is preserved. The coating produced with 80% $N_2$ is less homogenous, and cauliflower-like clumps are evident, surrounded by highly melted and then solidified splats. The surface clumps were on the order of the size of the feedstock particles. This observation suggests that the surface clumps may have been caused by unmelted or partially melted agglomerates of GDC or potentially due to increased splashing of hotter droplets in the higher-power plasmas.



**Fig. 5.** APS coatings produced with (a) 40% $N_2$ and (b) 80% $N_2$ plasmas.
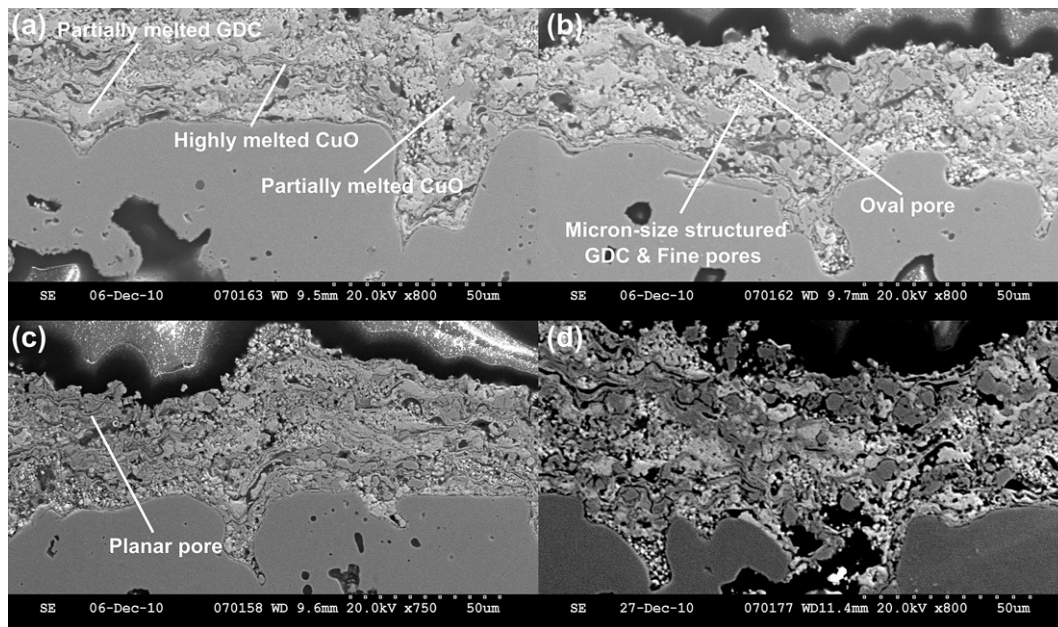
**Fig. 6.** Cross section SEM micrographs of coatings produced with (a) Cu–GDC, (b) 10 wt% Co, (c) 26 wt% Co, and (d) 50 wt% Co.

introducing porosity to the anode. It can be observed that the Cu in the Cu–GDC coating (Fig. 6(a)) was either partially melted in flight, resulting in the Cu retaining its original spherical shape, or highly melted, resulting in thin splats. It can be seen that the GDC is generally partially melted in flight in the fabrication of the Cu–GDC coating (Fig. 6(a)), although evidence of some highly melted GDC can be detected. The degree of melting of Cu and GDC is likely related to their particle sizes. Particles at the lower end of the sieved particle size range will tend to melt to a greater extent than particles at the high end of the sieved particle size range. It is also

possible that larger particles break up into smaller particles during the feeding process, resulting in a higher degree of melting in flight. It can also be observed in Fig. 6 that some of the GDC particles retain their finely-structured morphology, which is desirable to increase the triple phase boundary length.

Three types of porosity can be observed: fine pores, resulting from the fine-structured morphology of the GDC particles, oval-shaped pores, resulting from microstructural features of the partially melted sprayed particles and gaps between subsequently sprayed particles, and planar porosity, which is observed near
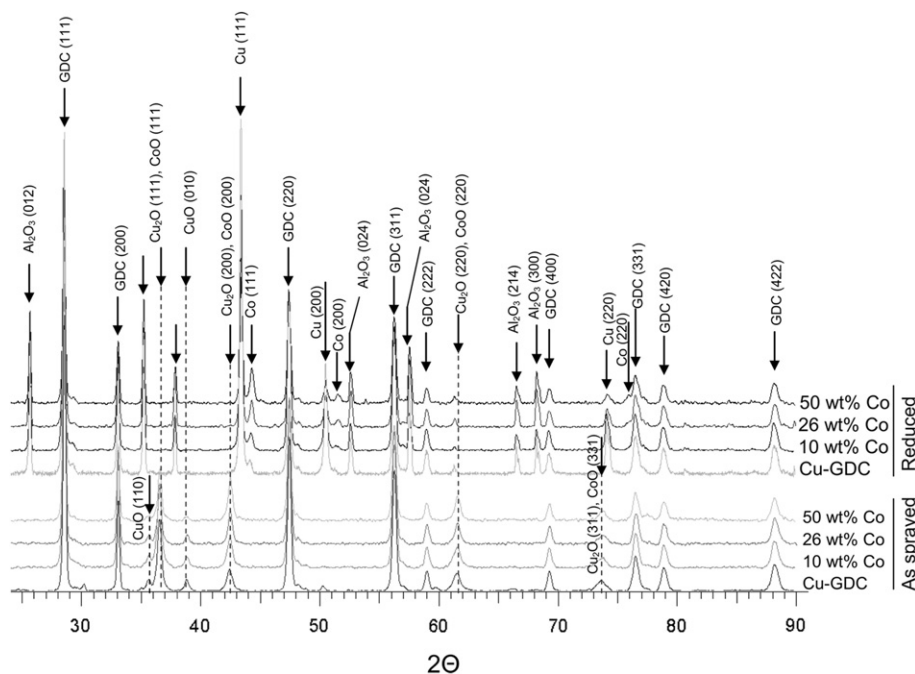


**Fig. 7.** XRD patterns of coatings produced from CuO–CoO–GDC powders sprayed with 40% $N_2$ – 60% Ar plasma. Y-axis represents X-ray intensity in arbitrary units. $Al_2O_3$ was used to calibrate peak position in the reduced coatings.
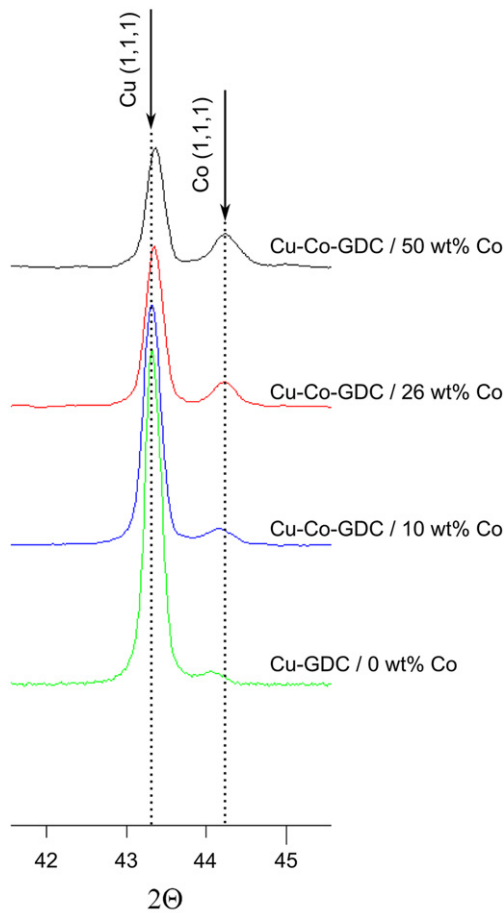
**Fig. 8.** XRD patterns of Cu–Co–GDC coatings sprayed with 40% $N_2$ − 60% Ar plasmas. *Y*-axis represents X-ray intensity in arbitrary units.

metallic particles and can be attributed to the decrease in volume due to reduction of metal oxide to metal.

Fig. 7 shows XRD patterns of as-sprayed CuO–CoO–GDC coatings produced with the spray parameters in Tables 2 and 3 and of reduced Cu–Co–GDC coatings. XRD patterns of the as-sprayed coatings show that the GDC remained cubic. XRD patterns after reduction demonstrate that the CuO and CoO were reduced almost completely to Cu and Co.

Fig. 8 shows XRD patterns of Cu–Co coatings from 42.5° to 45.5°. From the XRD patterns it is clear that the Cu and the Co peaks are shifted from their theoretical values. A previous study [9] utilizing wet ceramic processing to produce Cu–Co based anodes showed that a shift of the Cu peak in the XRD pattern to a higher angle was present, indicating the presence of some Co in the Cu-rich phase, consistent with expectations based on the Cu–Co phase diagram, in which the maximum dissolution of Co

in Cu is 0.71% [18,19]. In the same study [9], a Co peak was present in the XRD pattern at the position expected for pure Co metal.

In Fig. 8, it can be observed that both the Cu and Co peaks are shifted from the position of the peaks of pure Co and Cu metals. Due to the low solubility of these materials, it is more likely that the shifts of the peak positions are due, at least in part, to residual stresses in the coating rather than entirely to dissolution of the materials at the surface. Previous studies have shown that during plasma spray processing, a high level of in-plane tensile stress can develop within each splat during quenching after solidification, because thermal contraction of the splat is constrained by the underlying solid [20]. Depending on the orientation of the crystal lattice, this in-plane stress can cause an increase (tension) or a decrease (Poisson effect) of d-spacing between atomic planes, thus shifting the XRD peaks to a lower or a higher angle. It is likely that both residual stresses and some solid solution formation are present in the specimens investigated, with the shifting peak positions as a function of composition supporting the hypothesis of solid solution formation.

### 3.2.3. Porosity evaluation of Cu–Co–GDC coatings

Fig. 9 shows an SEM micrograph of a coating cross section and binary digitized images of the micrograph. Porosity was determined by adjusting the image threshold until the pore phase identified by the software best matched the pore phase that could be identified visually in the micrograph. Low grey scale solid features and high grey scale pores and micro-porosity can be identified in the image in Fig. 9(a). Fig. 9(b) shows a digitized binary image of the minimum estimated porosity, obtained by setting the grey scale threshold such that no solid feature that can be visually identified is included in the porosity estimate, for example, feature 3. However, it can be observed that some of the pore features having a high grey scale that are identified visually in Fig. 9(a) are not identified as pores, for example, features 1 and 2. Fig. 9(c) shows a digitized binary image of the maximum estimated porosity, obtained by setting the grey scale threshold such that all porous features that can be visually identified are included, for example, features 1 and 2. However, it can be observed that some of the solid features having a low grey scale that are identified visually in Fig. 9(a) are not identified as solids, for example, feature 3. Fig. 9(d) shows an image overlay of Fig. 9(b) and 9(c), visually demonstrating the extent of differences between the grey scale thresholds of minimum and maximum acceptable porosities (red). Fig. 9(e) shows a digitized binary image obtained with a grey scale threshold selected between the values shown in 9(b) and (c), resulting in an estimate of the porosity that corresponds well with the extent of the pore phase that can be visually identified in the micrograph.

Fig. 10 shows the average porosity values from 10 images of Cu–Co–GDC coatings for each Co loading obtained by image analysis using the optimized grey scale thresholds, and the calculated theoretical porosity values due only to reduction of CuO and CoO to Cu
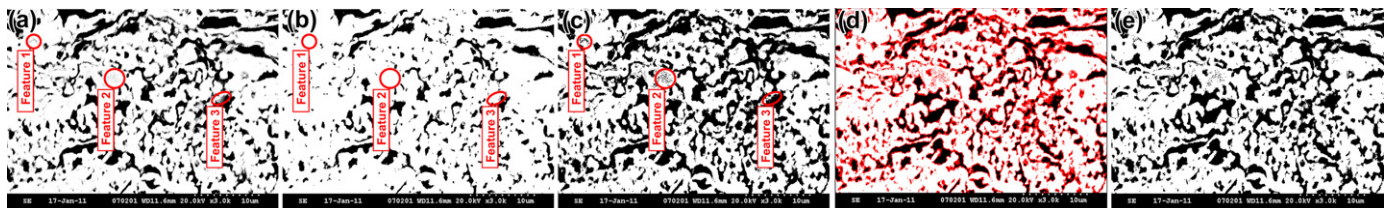


**Fig. 9.** (a) Coating cross section SEM micrograph and digitized binary images of (b) minimum estimated porosity (c) maximum estimated porosity, (d) Image overlay of minimum and maximum estimated porosities and (e) optimal estimated porosity.
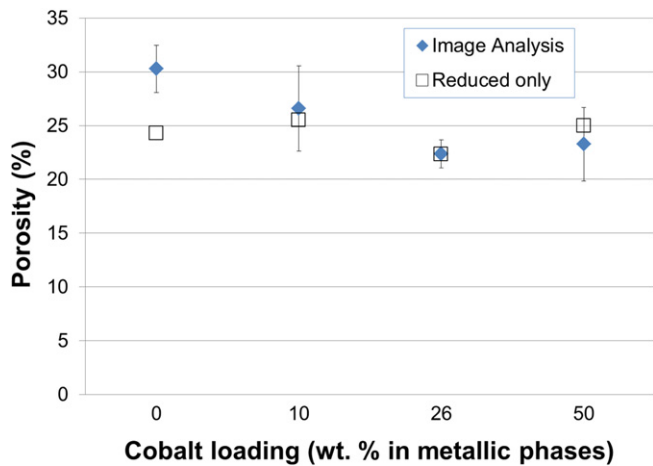
**Fig. 10.** Porosity of Cu–Co–GDC coatings with different Co loadings obtained by image analysis utilizing optimized grey scale thresholds.
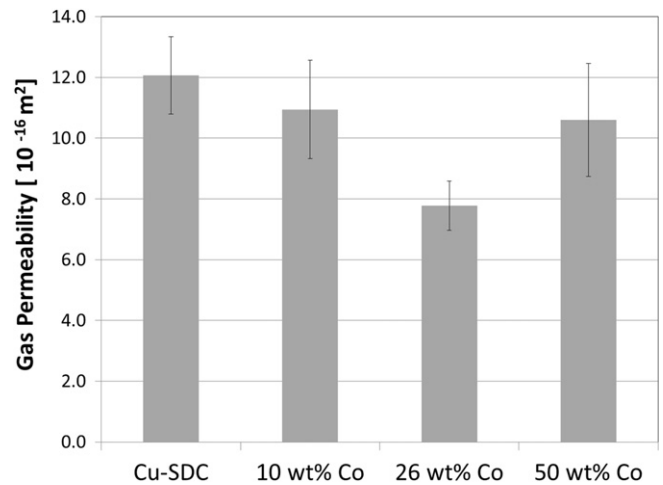


**Fig. 11.** Gas permeability coefficients of Cu–Co–GDC coatings with different Co loadings.

and Co. The theoretical porosity was determined from the molar composition obtained by EDX. The error calculated for image analysis is determined for each Co loading as the confidence interval of the average, with significance level $\alpha$ of 0.05.

The porosities calculated by image analysis utilizing optimized grey scale thresholds are within the range of 20–30%. These values are higher than the range reported by others for plasma spray processing of Cu–Co–YSZ SOFC anode coatings ([12]). This result can be attributed to the utilization of CuO and CoO feedstock powders and the porosity gain due to reduction of CuO and CoO to Cu and Co, and to partial melting of the GDC phase. The porosity values are also higher than typical plasma sprayed coating porosities, which are in the range of 5–15 vol%.

### 3.2.4. Gas permeability

The gas flux through the samples can be related to the permeation using Darcy's law (Eq. (2)):

$$\Phi_{\mathrm{gas}} = \frac{Q}{A} = \frac{-\kappa}{\mu}\left(\frac{P_b - P_a}{L}\right) \tag{2}$$

Here, $\Phi$ is the volumetric gas flux (m s$^{-1}$), $Q$ is the flow rate (m$^3$s$^{-1}$), $\kappa$ is the permeability (m$^2$), $A$ is the cross-sectional area to flow (m$^2$), $(P_b - P_a)$ is the pressure drop (Pa), $\mu$ is the dynamic viscosity (Pa s), and $L$ is the length over which the pressure drop takes place (m).

The normalized gas permeance is related to the gas flux through the sample and the corresponding pressure drop using Eq. (3)

$$\Lambda = \frac{d\Phi_{\mathrm{gas}}}{\left| dp_{\mathrm{app}} \right|} \tag{3}$$

In the case of two layers, substrate and anode, having pressure drops of $\Delta p_1$ and $\Delta p_2$ and fluxes $\Phi_1$ and $\Phi_2$, the total pressure drop $\Delta p_t$ is related to each layer's pressure drop using Eq. (4), and the total flux $\Phi_t$ is related to each layer's flux using Eq. (5),

$$\Delta p_t = \Delta p_{\mathrm{substrate}} + \Delta p_{\mathrm{anode}} \tag{4}$$

$$\Phi_t = \Phi_{\mathrm{substrate}} = \Phi_{\mathrm{anode}} \tag{5}$$

Algebraic manipulation of Eqs. (2)–(5) yields the anode permeability (Eq. (6)).

$$\kappa_{\mathrm{anode}} = \mu_{\mathrm{gas}} L_{\mathrm{anode}} \left( \frac{1}{\dfrac{1}{\Lambda_t} - \dfrac{1}{\Lambda_{\mathrm{substrate}}}} \right) \tag{6}$$

Using Eq. (6), the anode permeability can be calculated from the permeance of the substrate and the total permeance of the anode and substrate combination. The permeance in each case is calculated by applying various pressure drops and measuring the corresponding gas flow rates, which are then converted to gas fluxes. Least-squares fitting is used to calculate each gas permeance value.

Fig. 11 shows gas permeability coefficient values of Cu–Co–GDC coatings with different Co loadings. Both total porosity and gas permeability values do not correlate with the amount of Co present in the coating. Although CoO has a higher melting temperature than that of CuO, under the plasma energy conditions applied to deposit these coatings, the CoO does not play a role in generating increased porosity due to its extent of melting.

### 3.2.5. Carbon deposition

Visual observation of the coatings conducted after 3 h of exposure to 100% CH$_4$ at 700 °C showed that the coatings remained intact. Surface SEM analysis of these coatings did not reveal any visible cracks in the coatings or carbon deposits. However, EDX analysis performed on the coatings revealed that carbon was deposited on the coatings, with the weight fraction of carbon deposited increasing with the amount of Co in the coatings, as expected based on the catalytic activities of Cu and Co.

Table 5 summarizes the carbon formation data on Cu–Co–GDC coatings with various Co loadings obtained by the weight gain after exposure to dry CH$_4$ at 700 °C for 3 h. These results are comparable to those of carbon deposition experiments on Cu–Co based

**Table 5**
Carbon content in Cu–Co–GDC coatings after exposure to CH$_4$ at 700 °C for 3 h. Carbon content data of wet ceramics processed anode from the literature is shown for comparison purposes.

| Sample | wt% of carbon with respect to coating | Ref. 7 |
|---|---|---|
| Cu(100) | <0.1% | <0.1% |
| Cu(90)Co(10) | 0.43% ± 0.16% | 1% |
| Cu(74)Co(26) | 1.30% ± 0.08% | – |
| Cu(50)Co(50) | 1.92% ± 0.08% | – |
| Cu(10)Co(90) | – | 5% |

coatings produced by wet ceramic processing reported previously [7,9]. However, the extent of carbon deposition is related to the surface area of the Co and the ability of the $CH_4$ to permeate into the coating. Due to the fairly low permeability of these coatings, it is possible that the low carbon deposition is partially due to limited mass transport of $CH_4$ into the coating or due to low surface area of the cobalt phase.

## 4. Conclusions

Cu–Co–GDC coatings were produced by APS of CuO, CoO, and GDC agglomerates of micron-size particles. Adequate control of coating composition was achieved by determining the initial feedstock powder ratios required by using the absolute deposition efficiency of each material. A set of plasma spray parameters was identified to produce coatings with different Co loadings in which most of the GDC was partially melted and kept its fine structured morphology, as well as introducing sufficient porosity for use in an SOFC anode application. XRD patterns indicated possible inter-diffusion of Co and Cu. Co does not seem to have a role in increasing coating porosity due to the extent of melting of CoO under the APS conditions used in this study. The coatings demonstrated comparable stability against carbon formation as previously-fabricated wet ceramic produced anodes of similar composition reported in the literature, but were made with a simpler, single-step deposition process.

## Acknowledgements

## References

[1] N. Benoved, O. Kesler, J. Power Sources 193 (2009) 454–461.
[2] M.D. Gross, J.M. Vohs, R.J. Gorte, J. Mater. Chem. 17 (2007) 3071–3077.
[3] S. Jung, C. Lu, H. He, K. Ahn, R.J. Gorte, J.M. Vohs, J. Power Sources 154 (2006) 42–50.
[4] R.J. Gorte, J.M. Vohs, S. McIntosh, Solid State Ionics 175 (2004) 1–6.
[5] S. Park, R.J. Gorte, J.M. Vohs, Appl. Catal. A 200 (2000) 55–61.
[6] M.D. Gross, J.M. Vohs, R.J. Gorte, J. Electrochem. Soc. 154 (2007) B694–B699.
[7] S.-I. Lee, K. Ahn, J.M. Vohs, R.J. Gorte, Electrochem. Solid-State Lett. 8 (2005) A48–A51.
[8] S.W. Jung, J.M. Vohs, R.J. Gorte, J. Electrochem. Soc. 154 (2007) B1270–B1275.
[9] S.-I. Lee, J.M. Vohs, R.J. Gorte, J. Electrochem. Soc. 151 (2004) A1319–A1323.
[10] M.D. Gross, J.M. Vohs, R.J. Gorte, Electrochim. Acta (2007) 1951–1957.
[11] A. Benyoucef, D. Klein, O. Rapaud, C. Coddet, B. Benyoucef, J. Phys. Chem. Solids 70 (2009) 1487–1495.
[12] A. Benyoucef, D. Klein, C. Coddet, B. Benyoucef, Surf. Coat. Tech. 202 (2008) 2202–2207.
[13] C. Hwang, C. Yu, Surf. Coat. Tech. 201 (2007) 5954–5959.
[14] R. Hui, Z. Wang, O. Kesler, L. Rose, J. Jankovic, S. Yick, R. Maric, D. Ghosh, J. Power Sources 170 (2007) 308–323.
[15] W.M. Haynes, David R. Lide (Eds.), CRC Handbook of Chemistry and Physics, 91st ed., CRC Press Inc., Florida, 2012, pp. 4–57. pp. 4–62.
[16] C. Lu, W.L. Worrell, J.M. Vohs, R.J. Gorte, J. Electrochem. Soc. 150 (2003) A1357–A1359.
[17] Y. Gao, L.-T. An, C.-Q. Sun, Z.-J. Yan, J. Therm. Spray Technol. 13 (2004) 521–525.
[18] M. Palumbo, S. Curiotto, L. Battezzati, Calphad 30 (2006) 171–178.
[19] T. Nishizawa, K. Ishida, J. Phase. Equil. 5 (1984) 16.
[20] S. Kuroda, T. Fukushima, S. Kitahara, J. Therm. Spray Technol. 1 (1992) 325–332.